


Artifact suppression in readout-segmented consistent K-t space EPSI (RS-COKE) for fast ^1H spectroscopic imaging at 7 T

Amir Seginer¹ | Graeme A. Keith² | David A. Porter² | Rita Schmidt^{3,4} 

¹Siemens Healthcare Ltd, Rosh Ha'ayin, Israel

²Imaging Centre of Excellence, University of Glasgow, Glasgow, United Kingdom

³Department of Brain Sciences, Weizmann Institute of Science, Rehovot, Israel

⁴The Azrieli National Institute for Human Brain Imaging and Research, Weizmann Institute of Science, Rehovot, Israel

Correspondence

Rita Schmidt, Department of Brain Sciences, Weizmann Institute of Science, Rehovot, Israel.

Email: rita.schmidt@weizmann.ac.il

Purpose: Fast proton (^1H) MRSI is an important diagnostic tool for clinical investigations, providing metabolic and spatial information. MRSI at 7 T benefits from increased SNR and improved separation of peaks but requires larger spectral widths. RS-COKE (Readout-Segmented Consistent K-t space EPSI) is an echo planar spectroscopic imaging (EPSI) variant capable to support the spectral width required for human brain metabolites spectra at 7 T. However, mismatches between readout segments lead to artifacts, particularly when subcutaneous lipid signals are not suppressed. In this study, these mismatches and their effects are analyzed and reduced.

Methods: The following corrections to the data were performed: i) frequency-dependent phase corrections; ii) k-space trajectory corrections, derived from short reference scans; and iii) smoothing of data at segment transitions to mitigate the effect of residual mismatches. The improvement was evaluated by performing single-slice RS-COKE on a head-shaped phantom with a “lipid” layer and healthy subjects, using varying resolutions and durations ranging from $4.1 \times 4.7 \times 15 \text{ mm}^3$ in 5:46 min to $3.1 \times 3.3 \times 15 \text{ mm}^3$ in 13:07 min.

Results: Artifacts arising from the readout-segmented acquisition were substantially reduced, thus providing high-quality spectroscopic imaging in phantom and human scans. LCModel fitting of the human data resulted in a relative Cramer-Rao lower bounds within 6% for NAA, Cr, and Cho images in the majority of the voxels.

Conclusion: Using the new reference scans and reconstruction steps, RS-COKE was able to deliver fast ^1H MRSI at 7 T, overcoming the spectral width limitation of standard EPSI at this field strength.

KEYWORDS

MRSI, spectroscopic imaging, ultrahigh field

COI: A.S. is employed by Siemens Healthcare Ltd, Israel

This is an open access article under the terms of the Creative Commons Attribution-NonCommercial License, which permits use, distribution and reproduction in any medium, provided the original work is properly cited and is not used for commercial purposes.

© 2022 The Authors. *Magnetic Resonance in Medicine* published by Wiley Periodicals LLC on behalf of International Society for Magnetic Resonance in Medicine.

1 | INTRODUCTION

Proton MRS (^1H -MRS) in the brain is a well-established method that provides valuable diagnostic information in a range of diseases. ^1H -MRS information is utilized to characterize metabolic abnormalities in the human brain, assisting in cancer diagnostics¹ and in the assessment of neurological disorders^{2–5} such as Alzheimer's disease, schizophrenia, and depression. ^1H -MRS also provides new insights in the study of brain function^{6,7} by capturing changes in metabolite concentrations. ^1H -MRS of the human brain is typically performed at 1.5 T and 3.0 T; however, in recent years scanners operating at a magnetic field strength of 7 T have been approved for diagnostic applications of MRI and ^1H -MRS. At this higher field strength, ^1H -MRS applications have the advantages of increased SNR and an improved spectral resolution of metabolite resonances.^{6,8}

MRSI is an attractive method for performing ^1H -MRS for human studies as it provides simultaneously both metabolite and spatial information. Many of the MRSI methods are based on chemical shift imaging (CSI), which commonly results in a long scan duration. Recent developments in FID-MRSI^{9,10} have demonstrated good spatial resolution within acceptable scan durations by combining CSI with short TR and high acceleration using parallel acquisition with multi-channel receive coils. Additional directions for fast spectroscopic imaging also exist, including spiral,¹¹ concentric rings,¹² rosettes,¹³ and echo planar spectroscopic imaging (EPSI)¹⁴ schemes. The latter, EPSI, is a well-established fast MRSI technique^{15,16} in which an alternating readout gradient is used to simultaneously acquire both 1D spatial and 1D spectral information within a single shot. EPSI-based acquisitions have the potential to accelerate the acquisition while providing high-resolution MRSI. However, their high-resolution implementation at 7 T is hampered by hardware limitations that restrict the spectral width (SW).

One approach to increase the SW is to split the readout (RO) into several segments^{17,18} so that each RO gradient covers a smaller range of k-space (see Figure 1B). This allows the readout gradients to be shortened, which reduces the echo spacing (ESP) of the echo train (equivalent to the dwell time in an FID) and thus achieves a higher SW.

In practice, however, the effective dwell time is not represented by a single echo spacing because of the inconsistency between the readouts acquired under the positive and negative gradients.^{19,20} This arises both from hardware inconsistencies and from the opposite time evolution with respect to the k-position, k_x , along the RO direction; k_x increases or decreases with time according to the gradient sign. One way to resolve this is to analyze the positive-

and negative-polarity ROs separately^{21,22} and average the results. However, this effectively doubles the echo spacing and consequently halves the SW. To preserve the full SW, an alternative approach is used in this study based on the COKE (consistent K-t space EPSI) scheme.^{23,24} As shown in Figure 1, this technique adds alternating phase-encode (PE) blipped gradient pulses between the RO gradients and reverses the sign of both these PE blips and the RO gradients at every excitation. Consequently, the echo trains of *two* consecutive excitations can be reshuffled to give two new echo trains: one with positive RO gradients only and one with negative RO gradients only, each corresponding to a separate PE value (see Figure 1B–1D). Thus, two PEs are still acquired within two TRs, but the new echo trains are each internally consistent and have an effective dwell time of a single echo spacing, therefore providing the full SW. In practice, the COKE scheme trades the Nyquist ghost along the spectral dimension for a Nyquist ghost along the spatial PE direction.

In this study, the above two approaches were combined to create one sequence: the readout segmented COKE (RS-COKE). Initially, the application of RS-COKE was limited by ghosting artifacts of subcutaneous lipid signals.²⁵ These ghosts, along the spatial RO direction, affected the quality of spectra from brain–tissue regions. Although these contaminating signals can be reduced by lipid suppression techniques,^{26–28} these techniques can have an adverse effect on the metabolite signals of interest; furthermore, at 7 T, B_1 inhomogeneity makes the implementation challenging. Preliminary computer simulations (see Methods) verified two potential causes for these artifacts: The first was the lack of a suitable echo time shifting scheme²⁹ to match the off-resonance signal evolution between readout segments. The second was inconsistencies between the actual and expected k_x trajectory achieved by the RO gradients. The effect of similar trajectory errors in standard readout-segmented imaging sequences³⁰ is typically mitigated by applying empirical scaling corrections to RO gradient amplitudes. However, these measures are inadequate in the case of MRSI, where the low concentrations of brain metabolites render their signals highly sensitive to contamination by spatial ghosting from the relatively high concentration of lipids in subcutaneous fat.

2 | METHODS

Following the above insights of potential artifact sources, segment time shifts were incorporated in the sequence, and a procedure was developed to measure and reduce the RO-segment mismatches, leading to improved spatial and spectral quality (see Figure 2). The segment mismatches

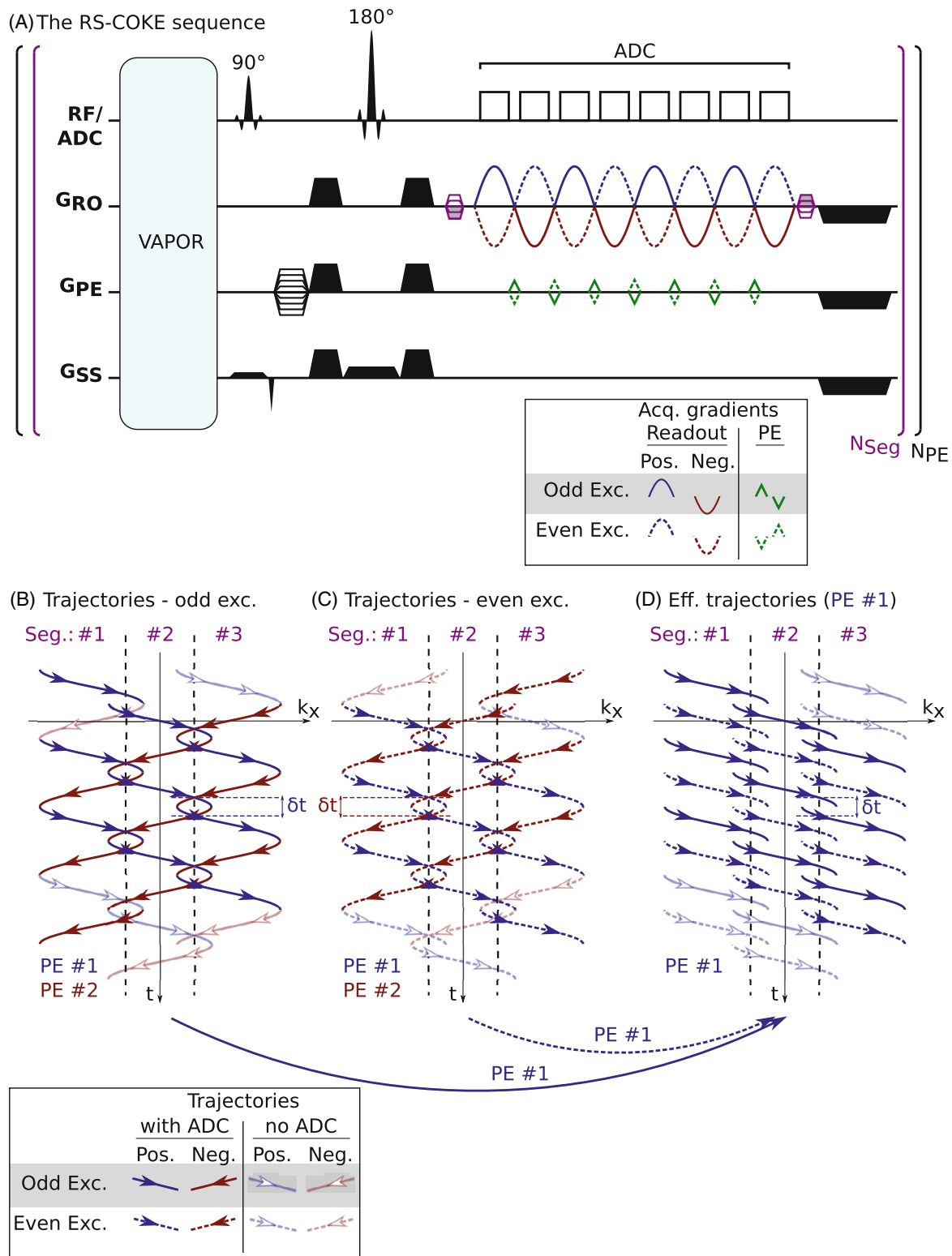


FIGURE 1 Schematic diagram of the pulse sequence and the acquired trajectories in RS-COKE. (A) A schematic diagram of the RS-COKE sequence and (B–D) the resulting $k_x - t$ trajectories. (B,C) are the trajectories of the odd and even excitations of a 3-segmented RS-COKE acquisition. Colors mark different PE lines (#1: blue; #2: red). Faint lines with hollow arrows mark gradients with data sampling switched off. All blue lines (PE #1) can be recombined from (B) and (C) into a consistent set (D) of acquisitions (same-PE and same-sign gradients). The same is done for PE #2 (not shown). The time gap δt is the gap between segments at the center of their overlap (vertical dashed lines). Further time-shifting the segments relative to each other can minimize the gap for either the positive or the negative gradient acquisitions but at the cost of a larger gap for the opposite acquisition gradient. PE, phase-encode; RS-COKE, readout-segmented consistent K-t space echo planar spectroscopic imaging.

were measured by adding two new reference scans to the sequence (extending the scan time by two TRs). The effect of the mismatch was then reduced through two main stages in the reconstruction: The first stage analyzed the new reference scans, deriving trajectory and timing corrections. The second stage employed these corrections in a regridding procedure used to handle the nonuniform sampling, including a smoothing of any residual intersegment inconsistencies.

The modified RS-COKE acquisition and processing scheme was examined in a 3D head-shaped phantom designed for MRSI evaluation, which included brain-mimicking metabolic content as well as a “lipids” layer. Finally, spectroscopic imaging with RS-COKE was examined in healthy human subjects, probing different SWs and number of segments.

The above steps, including the artifact simulations, are detailed next.

2.1 | Computer Simulations

A simple set of computer simulations was performed to investigate possible causes of imaging artifacts in a readout-segmented acquisition. A readout-segmented gradient-echo (GRE) acquisition was simulated, where each of its three segments was uniformly sampled in both time and k-space. The simulation modeled an axial view of the lipid layer as an elliptical ring. (See Supporting Information section S1 for more details on the modeling of the lipid layer).

Two variations to the sequence were tested: The first variation investigated the effect of a fixed time shift between consecutive segments. Firstly, data were generated for a zero time shift so that all 3 segments had the same TE. Secondly, data were simulated for a fixed time shift between the readout segments so that they were acquired at different TEs and behaved collectively as a single long readout (see Figure 3). The effect of the time shift variations was tested for both an on-resonance signal and a 1000 Hz off-resonance signal (approximating the lipid frequency offset at 7 T).

The second variation to the sequence investigated the effect of an unplanned overlap of the segments (or a gap between them). Such a mismatch between segments could arise in RS-COKE from inconsistent scaling of the amplitudes used for the sinusoidal RO gradients and their trapezoidal prephasers (see sequence diagram, Figure 1). In the simulation, the mismatch between segments was achieved by scaling the k_x value about the segment centers $k_{x,\text{center}}^{(s)}$ ($s = 1, 2, 3$) before shifting the centers. A scale of 1% was used, transforming the $k_x^{(s)}$ positions in segment s as follows:

$$k_x^{(s)} \rightarrow k_{x,\text{center}}^{(s)} + 1.01 \cdot \left(k_x^{(s)} - k_{x,\text{center}}^{(s)} \right). \quad (1)$$

This was compared to the perfect case.

2.2 | The RS-COKE sequence

Figure 1A shows the RS-COKE sequence as it was implemented on a 7 T Magnetom Terra (Siemens Healthcare, Erlangen, Germany). It is RO-segmented and employs sine-shaped RO gradients—unlike the trapezoidal gradients of conventional EPSI, as used today—as well as the COKE scheme. The sequence was designed so that neighboring RO segments have an overlap equivalent to 8 uniformly sampled points for the desired FOV L_x along RO, that is, a k-space range of $8 \cdot 2\pi/L_x$. Note that these extra points will not affect the duration of the scan as long as they fit within the desired echo spacing; otherwise, additional segments will be required, thus extending the total scan time. In addition to excitation and refocusing pulses, a VAPOR³¹ water-suppression module was used, consisting of 8 pulses with a total duration of 742 ms. Lipid suppression was not applied. The actual acquisition was preceded by 5 TRs of “dummy” scans to reach steady state.

Figures 1B–1D shows the k-space trajectories for the case of a 3-segment RS-COKE acquisition. Figures 1B,1C show the sinusoidal $k_x - t$ trajectory of the three segments. The trajectories have been time-shifted by one echo-spacing quanta with receivers switched off during some of the initial and final gradients, marked as light lines with empty arrow heads. With these skipped acquisitions, the recombined trajectories, as in Figure 1D, do not include superfluous acquisitions.

2.2.1 | Reference scans

In addition to the sequence described above, reference acquisitions were performed for the corrections described in sections 2.3.3–2.3.5. The reference scans were run on water, and in order to reach steady state they were preceded by five dummy scans on water. These dummy scans were in addition to the ones with *water suppression* preceding the actual scans performed.

The three reference scans were each a single segment acquisition but without water suppression or any PE (no PE prephaser and no COKE PE gradient blips). The frequency of the water suppression block was shifted to that of the lipids during the reference scan to reduce possible signal contamination by the off-resonance lipid signals.

The first reference, used for estimating time shifts and phase differences between odd and even echoes (with opposite polarity RO gradients), was similar to that

proposed for EPI in Ref. 32 and acquired the central RO segment (around $k_x = 0$).

The two additional reference scans were used to estimate inconsistencies between segments: one at the central RO segment and one at the adjacent segment. These scans included an *additional* separate but identical RO prephaser that shifted the segments so the center of their overlap region was at $k_x = 0$, where the signal is typically at a maximum. (See section 2.3.4 for the corrections derived from these scans.)

2.2.2 | Channel weights calibration

To estimate the weights when combining the signal from the different channels, an extra GRE sequence on water was scanned. The FOV and resolution of the GRE scan were similar, but not necessarily identical, to those of the RS-COKE scan (a user-interface limitation of the GRE sequence used).

2.3 | Reconstruction steps

2.3.1 | General reconstruction steps

The RS-COKE reconstruction was implemented in MatLab (MatLab 2018b and 2021a, MathWorks, Natick, MA) and included the following main steps:

- A Hann filter in k-space along both the RO and the PE dimensions;
- An exponential time apodization with decay constant of 0.1 ms;
- Fourier transformation along all dimension (RO, PE, and time), employing regridding for the nonuniform RO sampling;
- A weighted coil channel combination based on Ref.33.

Regridding was based on a convolution kernel³⁴ using a Kaiser-Bessel kernel to convolve the sampled signal at the desired on-grid k-positions (see Supporting Information section S1 for more details).

The coil combination weights were derived from the separate GRE image. Based on Ref.33, the weight given to each pixel at each channel was the complex conjugate of the GRE image (per channel and per pixel), normalized by the root-sum-of-squares of the channels at the GRE pixel. The signal was Hann-filtered (RO and PE) before the Fourier transform, and the image from each channel was interpolated to match the RS-COKE resolution.

Note that the Hann filter was used here instead of a Hamming filter. This was done due to the much faster decay of its ringing artifacts.³⁵ Nevertheless, both filters have the same downside of reducing the resulting resolution, halving it compared to the nonfiltered case, so the final image resolution is half that given by the reconstructed matrix. Apart for the Hann filter, no other processing was performed to reduce lipid artifacts.

2.3.2 | RS-COKE corrections — overview

The general reconstruction scheme above was supplemented with RS-COKE-specific corrections. A general flowchart of the modified reconstruction is shown in Figure 2, with correction steps marked in bold. The corrections are detailed below. (The effect of the different steps can be appreciated in Supporting Information Figure S1 in section S2, both for a phantom and for in vivo.)

2.3.3 | Even/odd inconsistencies: Nyquist ghosts

As in EPI,³² there may be inconsistencies between acquisitions with negative and positive RO gradient lobes. The only inconsistencies considered here are a time shift between the actual acquisition and the gradient waveform, as well as a fixed phase difference. These were found from the reference scan on water, without PE gradients, at the central RO segment (around $k_x = 0$). See Supporting Information section S1 for more details on the analysis.

Note that no actual correction was applied at this stage to the raw signals. The time shift was used within other corrections described below (trajectory corrections, and off-resonance phase corrections), see also the flowchart in Figure 2.

2.3.4 | Trajectory corrections (k_x and time t)

Any discrepancy between the planned and actual readout k-positions in the segments leads to artifacts when joining the segments. To correct for such discrepancies, the following relation was assumed between the actual sampled positions $k^{(s)}(t_n)$ of the n -th sample in segment s to the planned trajectory $k_{\text{ideal}}^{(s=0)}(t_n)$ for the center segment ($s = 0$)

$$k^{(s)}(t_n) = \eta \cdot k_{\text{ideal}}^{(s=0)}(t_n - \tau) + s \cdot \Delta k_{\text{seg}}, \quad (2)$$

where the two unknowns are the scaling parameter η and the absolute time shift τ between the actual acquisition and the gradient waveform (ideally $\eta = 1$ and $\tau = 0$), and

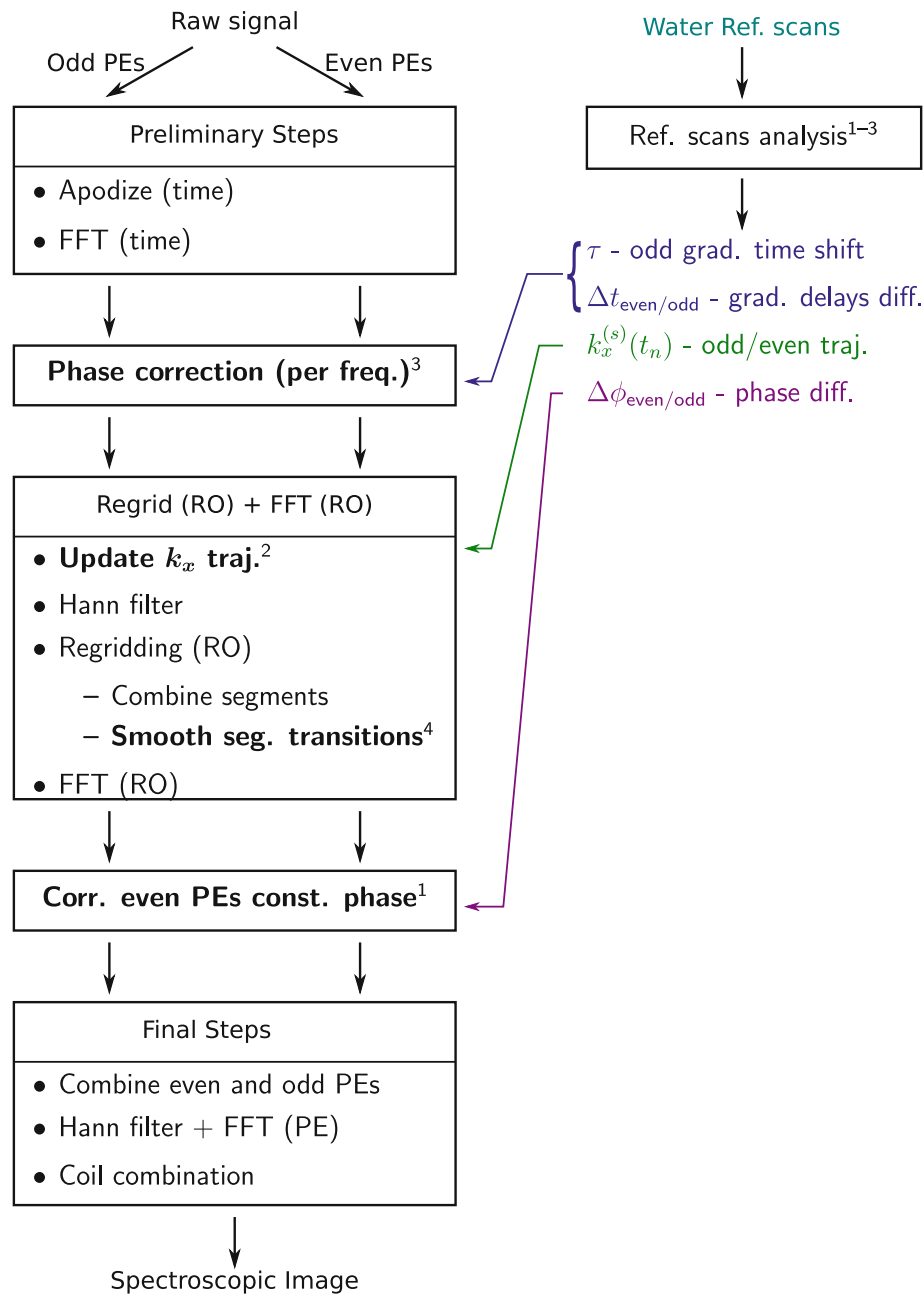


FIGURE 2 Schematic flowchart of the reconstruction, including correction steps. The odd and even PE lines (positive and negative RO gradients) are processed in parallel before they are combined in the final steps. The different parameters extracted from the water references (right) are used at different stages of the reconstruction, marked by arrows. Correction steps are marked in bold with superscripts marking the relevant section in the main text as follows: ¹even/odd inconsistencies: Nyquist ghosts, ²trajectory corrections k_x and time t , ³off-resonance inconsistencies, ⁴residual segment inconsistencies.

where Δk_{seg} is the increment between segments generated by the RO prephaser (seen at the start of the echo train in Figure 1).

The two parameters τ and η were determined from the 2-segment reference scan described above (two neighboring segments, $k_y = 0$, without PE blips, shifted to overlap around $k_x = 0$). From each scan, the odd acquisitions (positive gradient lobes) were separated out, a Fourier transform applied along the time axis, and the zero-frequency line of each segment extracted. This was followed by a root-sum-of-squares combination of the channels. With these two magnitude signals (from the two segments), the parameter pair τ and η for which the

signals best match at the overlap was found. See Supporting Information section S1 for more details on the fit performed.

Note that τ is an absolute shift, not a relative shift, and could be found because the sampling pattern $k_{\text{ideal}}^{(s=0)}(t_n)$ was nonuniform.

Once the shifts of the (analyzed) odd acquisitions were found, the same η scaling was used for the even acquisitions (opposite RO gradient sign). The even time shift used was a combination of the odd shift τ just found and the even/odd shift found earlier. Note that the even shift could be deduced separately from analyzing the even acquisition. This was not tested.

2.3.5 | Off-resonance inconsistencies

In order to consistently combine all the k_x segments for each phase-encode k_y value, phase consistency is required. This consistency is affected by the resonance frequency of each spectral component, as well as the timing of each data sample. This timing includes both the ideal prescribed timing (see Figure 1) and the deviations from this ideal as manifested in the trajectory corrections. The phase consistency corrections were divided into corrections within segments and between segments, as described below.

Phase inconsistencies within segments

For consistency within a segment, and especially between positive and negative RO gradients, the frequency matching the position in the spectrum was used to generate an appropriate linear phase to compensate for the phase evolution (before regridding). The sign of this linear phase was alternated between RO gradients of alternate polarity because the negative-polarity acquisitions were time-reversed to match the same k_x positions. The same correction was applied to all segments.

Phase difference between segments

For consistent merging of the RO segments, the phase must be continuous at the interface between the segments. Consequently, the phases of the data in each segment were adjusted, adding a frequency-dependent phase increment between adjacent segments so that the phase at the start of the segment would match that of the corresponding k_x data point in the previous segment. The phase increment used was based on the frequency at the given position in the spectrum and on the time shift between the two points. The evolution time used for each sampled point included the time shift correction τ in Equation 2 and the even/odd time shift found in the even/odd inconsistencies, section 2.3.3.

2.3.6 | Residual segment inconsistencies

Despite the above corrections, residual inconsistencies that still lead to artifacts are possible. To reduce these inconsistencies, the transitions between segments were linearly smoothed, as outlined below, to ensure signal continuity.

As a starting point, consider two segments continuously sampled in k -space, overlapping between $k_{\min}^{\text{overlap}}$ and $k_{\max}^{\text{overlap}}$. The signals of the two segments are given by $S_1(k)$ and $S_2(k)$, where $S_1(k)$ covers k s within the overlap and below it ($k \leq k_{\max}^{\text{overlap}}$), whereas $S_2(k)$ covers k s within the overlap and above it ($k \geq k_{\min}^{\text{overlap}}$). With these

assumptions, signal continuity at the edges of the overlap can be achieved by defining the following smoothed signal

$$S_{1,2}(k) = f_k \cdot S_1(k) + (1 - f_k) \cdot S_2(k), \quad (3)$$

$$k \in \left[k_{\min}^{\text{overlap}}, k_{\max}^{\text{overlap}} \right],$$

where f_k varies linearly with k , from one to zero (inside the overlap)

$$f_k \equiv \frac{k_{\max}^{\text{overlap}} - k}{k_{\max}^{\text{overlap}} - k_{\min}^{\text{overlap}}} \in [0, 1]. \quad (4)$$

In practice, the signals of the two segments are not continuously sampled but rather are at different discrete k s, thus Equation 3 could not be used and the smoothing was combined with the regridding to common k -positions. This was achieved by modifying—at the overlaps—the density compensation factors used in the regridding. (See Supporting Information section S1 for further details on how the smoothing was incorporated into the regridding.)

2.4 | Spectral analysis

Spectra in each voxel were fit with LCMoDel^{36,37} (v6.3) using simulated basis functions of 15 metabolites obtained by solving the full Liouville equations with in-house MatLab 2018 routines. The 15 metabolites were: aspartate (Asp), creatine (Cr), phosphocreatine (PCr), glycerophosphocholine (GCP), phosphocholine (PCh), glutathione (GSH), glucose (Glc), glutamine (Gln), glutamate (Glu), γ -aminobutyric-acid (GABA), sodium-lactate (Lac), myo-inositol (mI), N-acetylaspartate (NAA), N-acetylaspartylglutamate (NAAG), and taurine (Tau). The spectral fitting was performed in the range of 1.0–4.1 ppm. Following the fit, the resulting metabolite maps and the estimated relative CRLB (Cramer-Rao lower bounds) were collected. Note that for the short TE (14 ms) used here, a more accurate estimation could be found by including macromolecules in the set of basis functions³⁸; however, this was outside the scope of this work.

As the LCMoDel fitting was done separately per voxel, the resulting metabolite maps potentially hide pronounced changes in the lipids and the baseline between neighboring voxels, thus hiding lipid contamination and lipid ghosting artifacts. Metabolite images were therefore also created using straightforward integration over each of the metabolite peaks (the integration range is specified in the figure captions). Direct integration is more sensitive to lipid contamination and ghosting artifacts, highlighting their presence (as well as being much faster), and is therefore important for visual inspection.

2.5 | Experiments

The experiments were performed on a 7 T MRI system (Magnetom Terra, Siemens Healthcare) using a commercial 1Tx/32Rx head coil (Nova Medical, Wilmington, MA). The RS-COKE acquisitions were accompanied by scout scans for localization, a high-resolution GRE scan as a reference, and low-resolution GRE scans used to generate coil combination weightings.

Note that as RO sampling was nonuniform, the reported acquisition matrices represent the theoretical resolution for the k-space region covered. As the sequence was implemented so that segments have an overlap of 8 sample points (after regridding), each segment was acquired with 4 extra samples at each edge. Thus, the acquisition matrixes were always 8 samples larger along the RO compared to the reconstruction matrices.

2.5.1 | 3D head-shaped phantom imaging

A 3D-printed, head-shaped phantom designed for 7 T was used.³⁹ The phantom included 3 subsections, mimicking brain, muscle, and lipid tissues, respectively. It included an agar “brain” region with metabolites and an oil-filled “lipids” layer. The brain-mimicking metabolites for spectroscopy comprised the following solution: 10 mM L-glutamic acid, 10 mM Cr and PCr (together Cr + PCr), 8 mM myo-inositol, 2 mM gamma-aminobutyric acid, 2 mM Cho, 5 mM sodium lactate, and 12.5 mM NAA. Potassium dihydrogen orthophosphate was used as a buffer to achieve pH of ~7 (typically titrated using ~2.13 g/L sodium hydroxide pellets). For further details, see Ref. 39.

Scan parameters for the RS-COKE acquisition were: 3 RO segments, ESP = 0.36 ms (SW = 2778 Hz), FID duration 106 ms, FOV (RO × PE) 200 × 250 mm², acquisition matrix 56 × 64, reconstructed matrix 48 × 64, in-plane reconstructed resolution 4.1 × 3.9 mm², slice thickness = 15 mm, TR/TE 2000/14 ms, and scan duration 6:08 min. Low-resolution GRE scan parameters were FOV 200 × 250 mm², in-plane reconstructed resolution 4.1 × 3.9 mm², slice thickness 5 mm, TR/TE 50/2 ms, and scan duration 5 s.

2.5.2 | Human imaging

All scans were carried out in accordance with the Weizmann Institute of Science (Rehovot, Israel) guidelines and regulations, and were performed according to procedures approved by the Internal Review Board of the Wolfson Medical Center (Holon, Israel) after obtaining informed

suitable written consents. Three volunteers were scanned with the following four RS-COKE scans:

- i. Three RO segments, ESP = 0.34 ms (SW = 2941 Hz), FID duration 217 ms, FOV (RO × PE) 260 × 300 mm², acquisition matrix 71 × 64, reconstructed matrix 63 × 64, in-plane reconstructed resolution 4.1 × 4.7 mm², slice thickness = 15 mm, TR/TE 1700/14 ms, and scan duration 5:49 min.
- ii. The same as (i) above, but with 5 RO segments, with acquisition matrix 68 × 64, reconstructed matrix 60 × 64, in-plane reconstructed resolution 4.3 × 4.7 mm², and scan duration 9:26 min.
- iii. The same as (ii) above but with a larger acquisition matrix 93 × 90 and reconstructed matrix 85 × 90, resulting in-plane reconstructed resolution 3.1 × 3.3 mm² and scan duration 13:07 min.
- iv. The same as in (i) but with ESP = 0.28 ms (SW = 3571 Hz).

The low-resolution GRE scan parameters were: FOV 260 × 300 mm², in-plane reconstructed resolution 4.1 × 4.7 mm², slice thickness 5 mm, TR/TE 50/1.8 ms, and scan duration 4 s.

The high-resolution GRE scan parameters were: FOV 260 × 300 mm², in-plane reconstructed resolution 1.6 × 1.6 mm², slice thickness 5 mm, TR/TE 50/2 ms, and scan duration 11 s.

3 | RESULTS

3.1 | Simulation results

Figure 3 summarizes the results of simulations examining the ringing artifacts in a readout-segmented acquisition for an annulus object that mimics the subcutaneous lipid layer around the brain. Figure 3A shows an acquisition in which each RO segment was acquired at the same time relative to the excitation. Both on- and off-resonance cases are shown, where the off-resonance case mimics the lipid signal. Figure 3B shows an acquisition with incremental time shifts Δt of the segments ($\Delta t = s \cdot \text{ESP}$, with s the segment number) to achieve a continuous temporal evolution along the segmented k_x direction. Only the off-resonance case is shown. The effect of the change between Figure 3A,3B is clearly seen in Figure 3C, comparing the two results along a cross section.

Figure 3D shows the effect of scaling the RO amplitude (without scaling the corresponding prephasing gradients), simulating a scaling error between the prephasing and the readout. The plot on the right of Figure 3D exemplifies the effect by showing the signals—with and without the stretch—along a cross section.

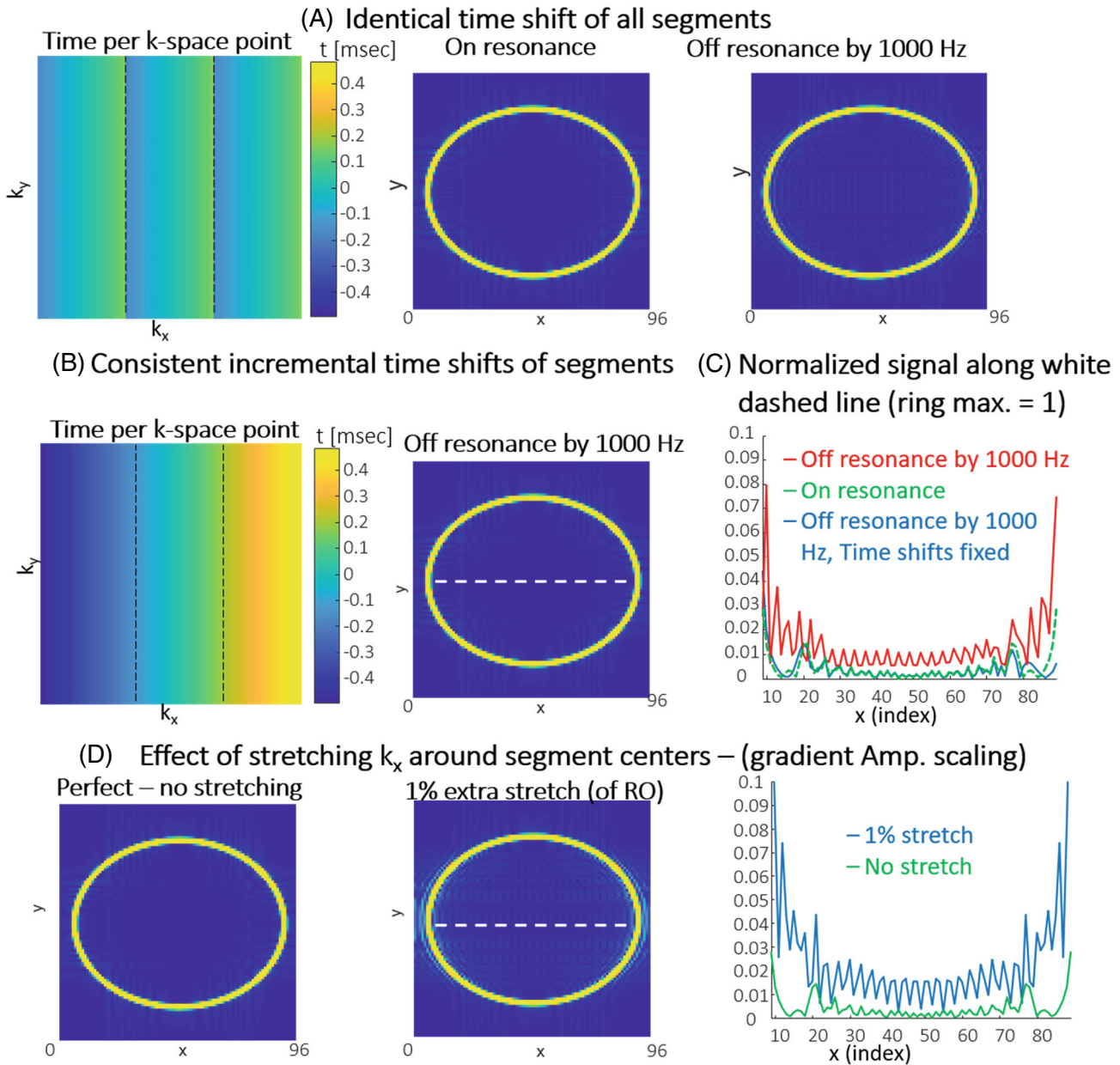


FIGURE 3 Simulated ringing artifacts in a readout-segmented acquisition for an annulus object mimicking the subcutaneous lipid layer in the head. (A) Each segment acquisition starts at the same delay from the excitation; both on- and off-resonance cases are shown (off-resonance mimics the lipid signal). (B) Acquisitions with incrementally time-shifted segments to achieve an effective continuous temporal evolution within each 3-segment PE line. (C) Signal ringing along an image-domain line (white, dashed) inside the annulus for cases (A) and (B). (D) Effect of scaling the RO amplitude (but not the corresponding prephasing gradients); a stretching that can occur between the segments. For simplicity, simulations used equidistant k-space points instead of the nonuniform sampling (sine-shaped gradients) used in the actual scan. RO, readout.

In this simulation, the dominant artifacts come from the incorrect gradient amplitude scaling (of 1%). The case of time-shifted segments for the off-resonance signal also results in significant artifacts. In this synthetic simulation, even the perfect case (on resonance, no shifts or amplitude error) has minor Gibbs ringing artifacts. In practice, these would be less apparent in human imaging due to noise, irregular edges, and partial volume along the slice

dimension (effectively smoothing the edge within the 2D slice).

3.2 | Phantom results

The results of RS-COKE acquired in a 3D head-shaped phantom designed with a “lipids” layer and brain-mimicking metabolites are shown in Figures 4–6.

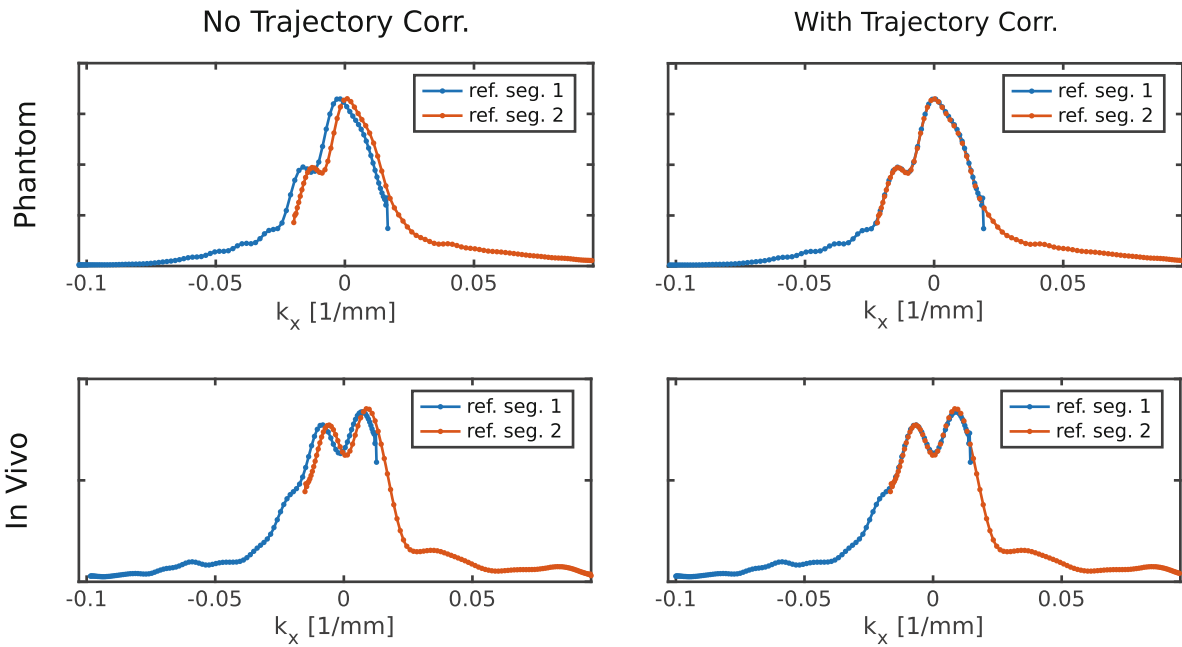


FIGURE 4 Signals from the trajectory reference scans on water (left: before trajectory correction; right: after; top: phantom scan; bottom: a scan performed in vivo). Signals shown are the zero-frequency component of the reference scans raw data (after apodization and an FT along time). The stray blue points, even after correction, are probably transients due to switching of the receivers on/off, and were disregarded (the first and last 4 samples were always discarded in the analysis). FT, Fourier Transform.

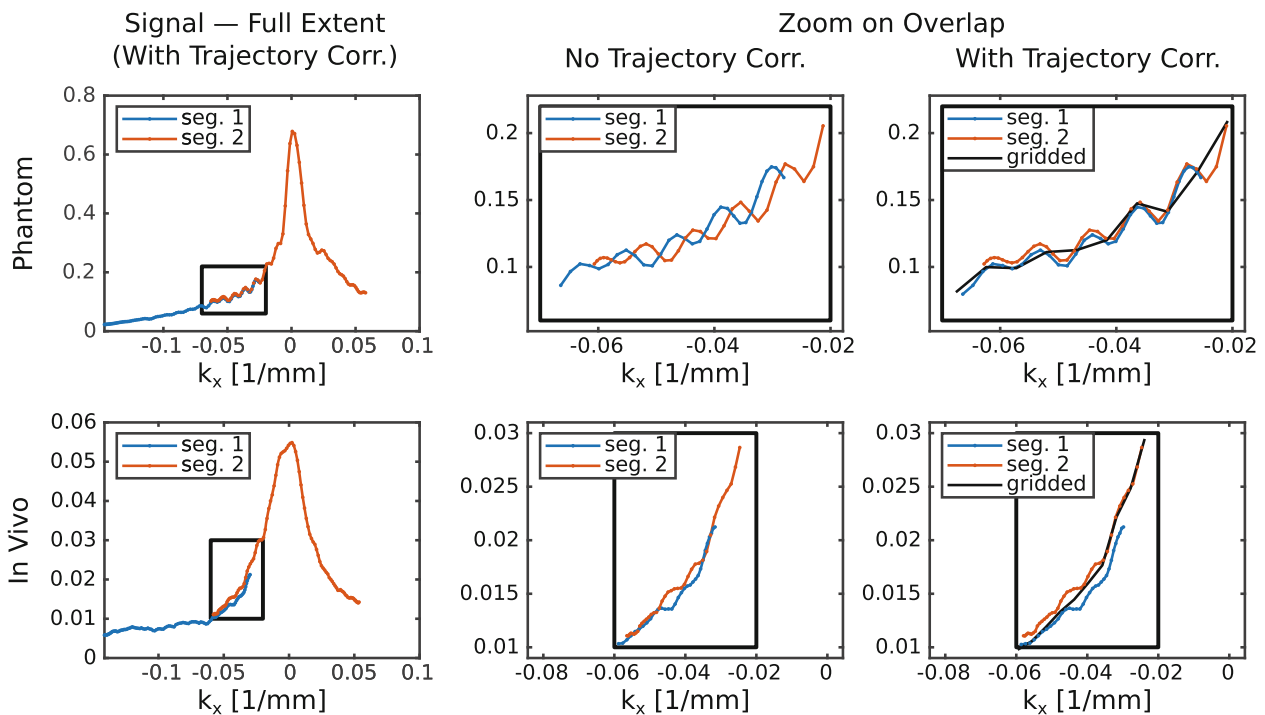


FIGURE 5 The effect of the trajectory correction on the signal at the transition between overlapping segments (top, phantom example; bottom, data acquired in vivo). The full extent of the signals is shown to the left, with zooms into the overlap shown in the middle and on the right (middle before correction and right after correction). The corrected signals are overlaid with the gridded signal (black), which smooths the transition (see main text). After correction, the signal mismatch in vivo is mostly in amplitude, probably mainly due to physiological changes. Signals are shown for $k_y = 0$ and for the dominant frequency (lipids)

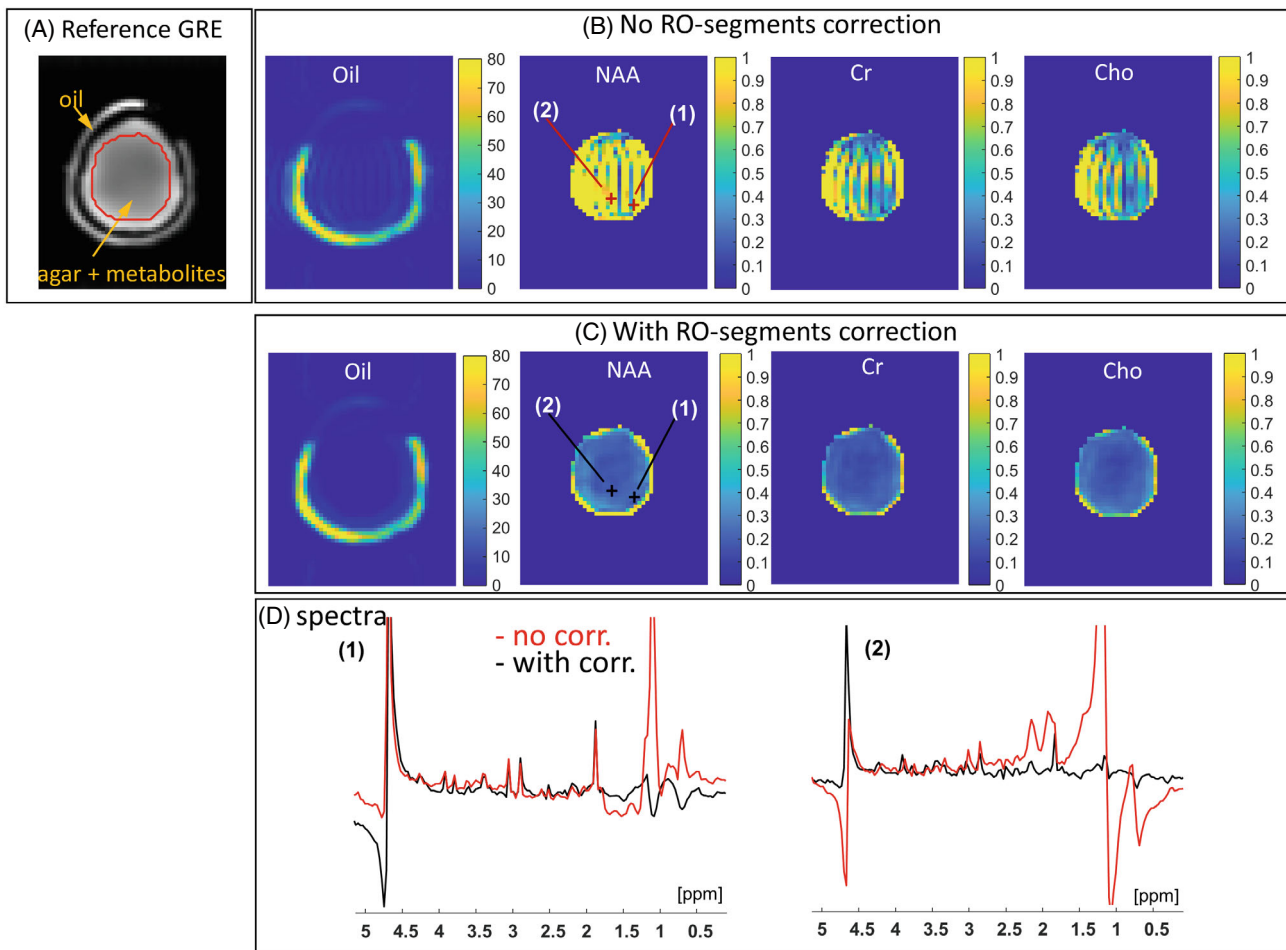


FIGURE 6 Phantom RS-COKE results without and with RO-segments corrections. (A) A GRE scan at the MRSI slice position (used to calibrate coil combination weights). (B) Spectral images for “lipids” (oil), NAA, Cho, and Cr, without trajectory corrections or smoothing of transitions. (C) Same as (B) but with corrections. (D) Spectra at the positions (1) and (2), marked on the NAA images. Red spectra are without the corrections and black spectra have been corrected. Spectra are displayed as the real part after a 3×3 voxel average. Images are the magnitude after integration over the complex spectrum in the corresponding voxel, with the lipid image summed over 227 Hz and the metabolites over 116 Hz. The lipid images scale is $\times 80$ that of the metabolite images. The scaling of the intensity in the images was chosen to highlight the artifacts. The same scaling was used for the top (without correction) and bottom (with corrections) images. GRE, gradient echo.

Figure 4 (top) shows the zero-frequency signals of the phantom’s 2-segment reference scan, comprising two consecutive RO segments, shifted in k -space (by modifying the prephasing gradient) to overlap around $k_x = 0$. On the left are the measured signals using the nominal RO k -trajectory in each segment, whereas on the right are the signals after the trajectories have been corrected according to Equation 2, with τ and η such that the signals best match. The signals match well after the correction.

Figure 5 (top) shows phantom sample data for two segments from the actual acquired signal before and after trajectory correction; signals are at $k_y = 0$ for the spectral frequency with the strongest signal (“lipids”). The corrected signals are overlaid with the gridded signal

(black), which smooths the transition. While the trajectory correction aims to align the segments along k_x , the transition smoothing compensates for amplitude differences and any other residual mismatches.

Images of the “lipids”, NAA, Cr, and Cho peaks are shown in Figure 6 before and after the applied corrections. The RO-segmentation ringing artifacts are clearly seen before the correction, while after the correction a uniform phantom distribution is revealed (as expected). Figure 6D shows the spectra from two voxel locations: in a clean region (1) and on the ring artifact (2). While the first shows a mild difference between metabolite peaks before and after correction, the second case (voxel close to the lipid) shows a significant improvement.

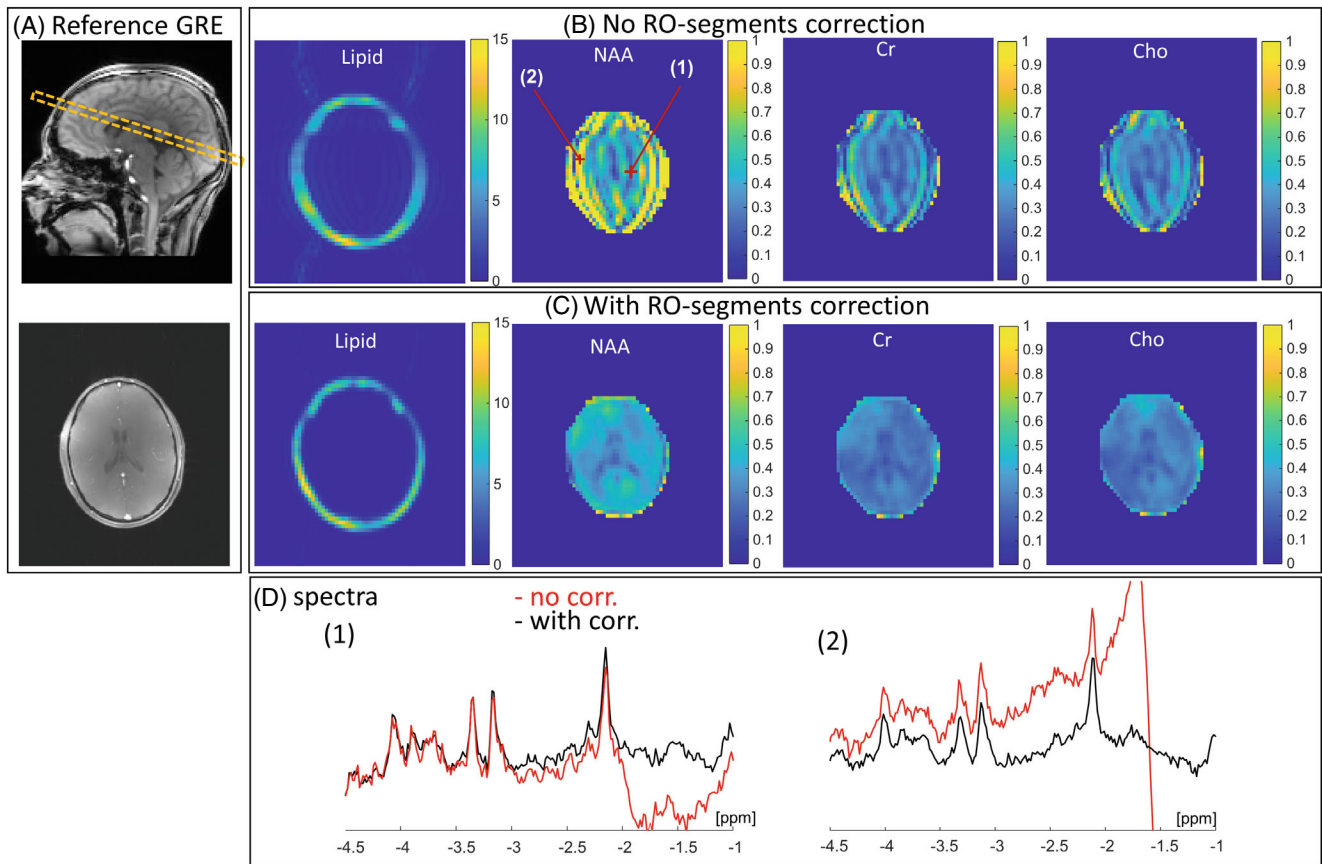


FIGURE 7 In vivo RS-COKE results without and with RO-segments corrections. (A) Images for reference: a localizer showing the slice position and a high-resolution GRE scan at the slice (with IR for T_1 weighting). (B) Spectral images of lipids, NAA, Cho, and Cr, without trajectory corrections or smoothing of transitions. (C) Same as (B) but with corrections. (D) Spectra at the positions (1) and (2), marked on the NAA images. Red spectra are without the corrections and black spectra have been corrected. Spectra are displayed as the real part after a 3×3 voxel average. Images are the magnitude after integration over the complex spectrum in the corresponding voxel, with the lipid image summed over 227 Hz and the metabolites over 116 Hz. The lipid images scale is $\times 15$ that of the metabolites. The scaling of the intensity in the images was chosen to highlight the artifacts and the features. The same scaling was used for the top (without correction) and bottom (with corrections) images.

3.3 | Human imaging results

Figure 4 (bottom) shows the zero-frequency signals from a 2-segment reference scan acquired in vivo. Again, the measured signals using the nominal RO k-trajectories are on the left, while the signals after the trajectory corrections are on the right.

Figure 5 (bottom) shows the effect of the trajectory correction in vivo. The signals shown are from the actual scan (not the reference scan) at $k_y = 0$ for the spectral frequency with the strongest signal, corresponding to the lipids.

Figure 7 shows images and spectra acquired from a healthy human subject using RS-COKE. Data are shown before and after corrections. Images are shown for the lipids, NAA, Cr, and Cho peaks. The images after correction show clear features of the ventricles and other anatomical features. Figure 7D shows spectra in two

representative voxels, with a significant reduction in artifact following the applied correction. For comparison, Figure S2 also shows LCMoel fitting of this dataset before and after correction. The LCMoel NAA map, from the data before correction, shows fewer artifacts than the matching NAA image of Figure 7 (generated by simple integration). Nevertheless, the average CRLB in the brain before correction is high (34.4%) compared to the same map after corrections (5.5%).

Figures 8 and 9 show the four RS-COKE scans acquired with two different SWs, 3 and 5 RO segments, and at different spatial resolutions. All four scans show clean spectra with a low level of lipid contamination. Five segments, instead of 3, can be used to increase the SNR for the same spatial resolution (second column in Figures 8 and 9) or to increase the resolution (third column). High SWs of ~ 3600 Hz can be achieved with RS-COKE even with 3 segments (fourth column). The CRLB of the LCMoel

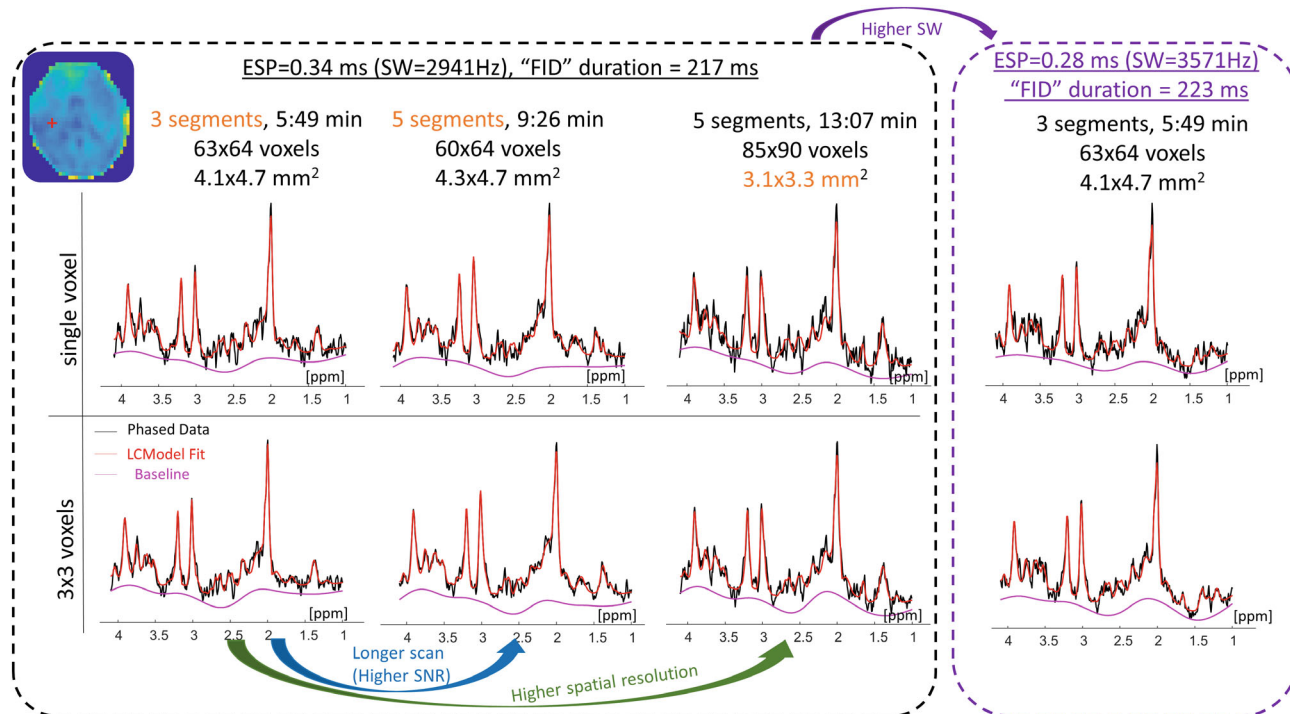


FIGURE 8 Spectra from RS-COKE with different spectral width, number of segments, and spatial resolution. Left, spectra from three scans with ESP = 0.34 ms (SW = 2941 Hz): (i) 3 segments and 63×64 reconstructed voxels ($4.1 \times 4.7 \text{ mm}^2$) in 5:49 min, (ii) 5 segments and 60×64 reconstructed voxels ($4.3 \times 4.7 \text{ mm}^2$) in 9:26 min, and (iii) 5 segments and 85×90 reconstructed voxels ($3.1 \times 3.3 \text{ mm}^2$) in 13:07 min. Right, scan (iv) with ESP = 0.28 ms (SW = 3571 Hz) and the rest as in (i). The top row shows the LCMoDel fitting for a single voxel, the bottom row for an average of 3×3 voxels. The image at the top-left corner shows the NAA image from Figure 6 with the location of the voxel marked by a red plus symbol. ESP, echo spacing; SW, spectral width.

in the central region is within 6%, increasing only in the ventricles and near the lipid layer.

Figure 10 shows LCMoDel metabolites maps and CLRB images of the NAA, Cr, and Cho, as well as the (glutamate + glutamine)/NAA ratio for two in-plane resolutions ($4.1 \times 4.7 \text{ mm}^2$ and $3.1 \times 3.3 \text{ mm}^2$ (reconstructed), corresponding to scans (i) and (iii) in Methods).

4 | DISCUSSION

The RS-COKE pulse sequence, incorporating readout-segmented EPSI and alternating PE blips for consistent k-t space acquisition, offers fast spectroscopic imaging and high spatial resolution for human application at 7 T. The method can mitigate the spectral-width limitation at 7 T and provides a coherent phase evolution that avoids Nyquist artifacts in the spectra. However, the method is susceptible to ringing artifacts along the RO direction. This phenomenon is known from standard imaging applications of readout-segmented EPI, where simple mitigations such as a system-specific RO gradient scaling can achieve a sufficient suppression of the artifact. However, in the case of EPSI, the residual ringing

artifact is detrimental to spectral quality. This is especially evident when the lipid suppression is switched off as the off-resonance lipid signal is then high compared to that of brain metabolites. These signals emanate from the subcutaneous scalp region, which forms a *sharp* ring around the brain further amplifying the ringing artifact.

In this study, we have introduced a method to minimize this ringing artifact by correcting k-space trajectory inconsistencies between the RO segments. The correction uses a short adjustment scan at the start of the acquisition to provide data that are specific to the scan protocol being used and fits these data to a mathematical model to estimate and correct the trajectory difference between adjacent segments. In addition, the method applies signal smoothing at RO-segment transitions and a phase correction that is both frequency- and segment-specific. In conjunction, these processing steps were shown to substantially reduce artifacts in spectra and metabolite maps and provide a powerful tool for correcting the segment-to-segment inconsistencies without the need for a prior calibration of individual scan protocols.

The results show adequate signal correction, both in the dedicated 3D head-shaped phantom and in human scanning. As in FID-MRSI without lipid-suppression,^{9,40}

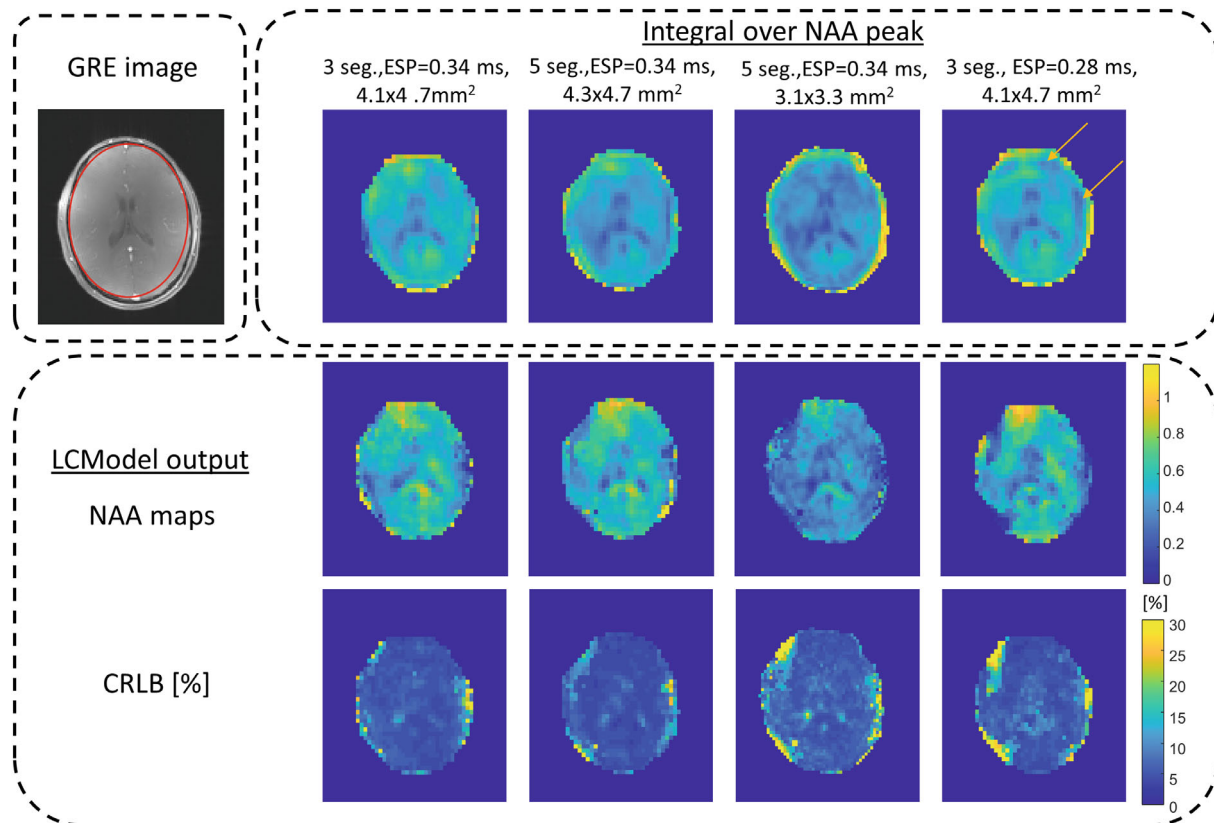


FIGURE 9 NAA images from RS-COKE for varying scan parameters: SW, number of segments, and spatial resolution. From left to right: the first three with $ESP = 0.34$ ms ($SW = 2941$ Hz) having: (i) 3 segments and 63×64 reconstructed voxels (4.1×4.7 mm²) in 5:49 min, (ii) 5 segments and 60×64 reconstructed voxels (4.3×4.7 mm²) in 9:26 min, (iii) 5 segments and 85×90 reconstructed voxels (3.1×3.3 mm²) in 13:07 min, and the last scan (iv) with $ESP = 0.28$ ms ($SW = 3571$ Hz) but otherwise the same as (i). The top row shows the NAA images integrated over 116 Hz around the NAA peak. The middle row shows the LCModel-estimated NAA maps, and the bottom row shows the corresponding CRLB maps. The image at the top-left corner shows the high-resolution reference GRE image with the outline for the mask used on the NAA images marked in red. The arrows in the top-right image point to residual artifacts in the integral image: one in the PE direction and one in the readout direction, which were removed with the LCModel fitting. Each of the integral images was scaled separately to visualize the features. The metabolite maps (based on LCModel) were all scaled the same, normalized to the maximum of the right most image. The FOV of the images was cropped to reduce surrounding empty space. CRLB, Cramer-Rao lower bounds.

this method allows the acquisition of metabolite maps without the need for outer-volume suppression, thus reducing the specific absorption rate and providing full-slice coverage. The leakage of the unsuppressed lipid signal into the brain regions was minimized by applying a Hann filter in k-space. Using the Hann filter instead of a Hamming filter practically removed lipid ringing artifacts well within the brain without any other lipid removal processing. Although applying the filter lowers the final resolution of the image, it is a frequently used tradeoff, even when additional post processing is used to remove the lipids signal.^{9,40}

The images acquired in vivo still occasionally suffer from artifacts along the PE direction, which are most likely due to motion and breathing. The LCModel fitting is more immune to these artifacts because it removes the fluctuations that appear as the spectra baseline.

This study has focused on a single slice-selective MRSI acquisition. RS-COKE can be extended to whole-brain studies with either multi-slice or 3D phase encoding. This can be achieved by reducing the TR using a shorter water suppression module, as was previously reported.⁹ With acquisition of ~ 200 ms, as in this study, a TR of ~ 300 ms could be achieved. In this case, 3D phase-encoded whole brain scan with 10 mm resolution and 3 segments could be acquired in ~ 12 min (including 12 phase-encoding points). The multi-slice configuration can incorporate acceleration method using multi-band pulses, which was already demonstrated with the COKE implementation at 3 T.^{41,24} In this case, 12 slices using acceleration factor of 2 would be acquired with a similar scan time to that in this study.

This whole-brain extension should also consider SNR efficiency, which depends on the trajectory traversed and

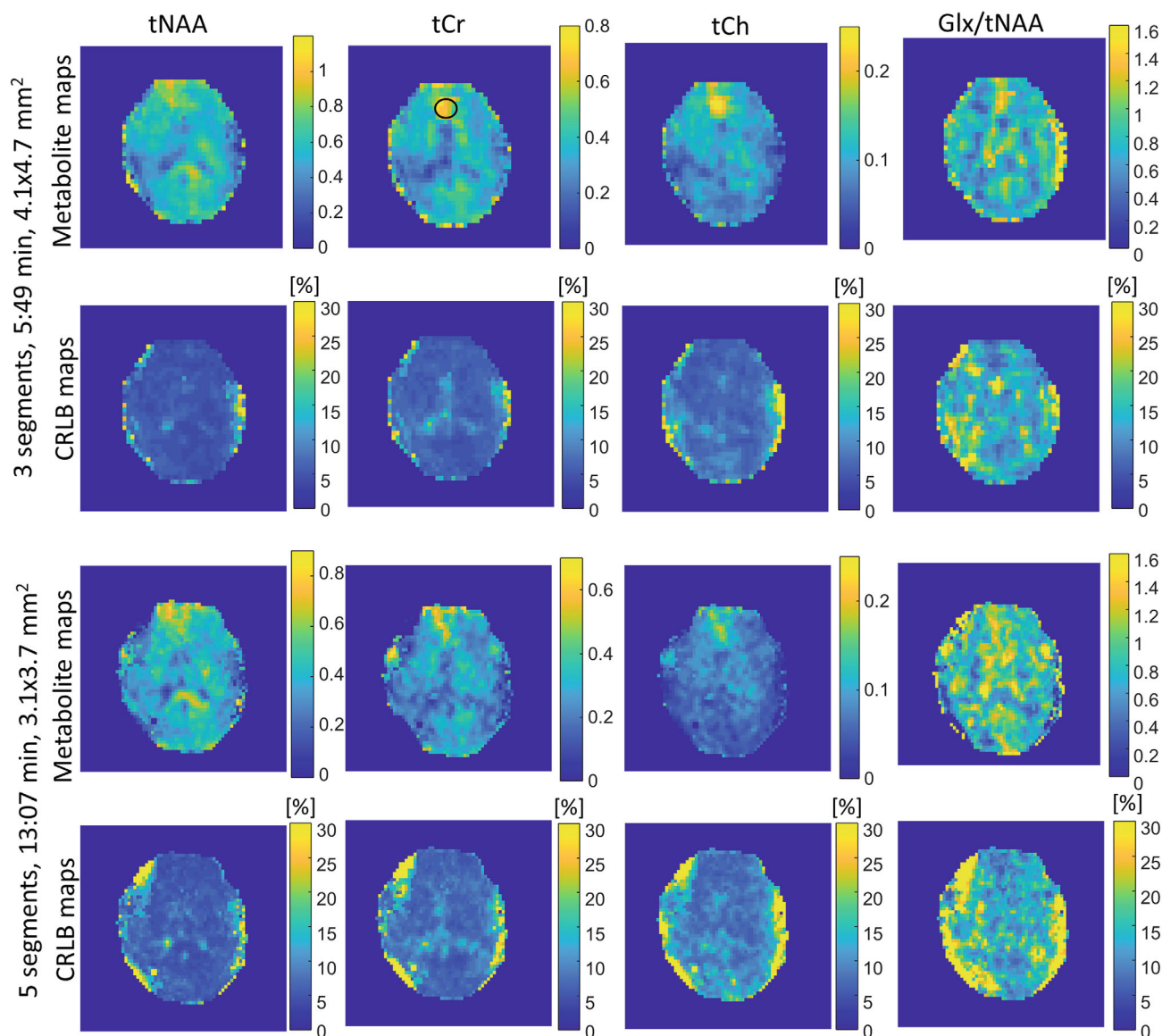


FIGURE 10 Metabolite maps from LCMoDel: NAA, Cr, Cho, and Glu + Gln/NAA ratio. The images shown are for scan (i): ESP = 0.34 ms (SW = 2941 Hz), 3 segments, 63×64 reconstructed voxels ($4.1 \times 4.7 \text{ mm}^2$) in 5:49 min; and for scan (iii): 5 segments, 85×90 reconstructed voxels ($3.1 \times 3.3 \text{ mm}^2$) in 13:07 min. The metabolite maps and the corresponding CRLB maps are shown. The color bars of the metabolite maps were chosen to highlight the features for each metabolite. The maps were normalized the same as in Figure 9. The black overlay highlights a region with high B_0 inhomogeneity. The FOV of the images was cropped to reduce surrounding empty space.

the desired filter (Hann filter in this case). Based on Kasper et al.,⁴² the SNR efficiency of RS-COKE and EPSI is examined in the Supporting Information section S4. For comparison with EPSI without temporal interleaving, having the same SW, a slightly larger FOV than used in the in vivo scans was examined. The SNR efficiency of RS-COKE and EPSI (without temporal interleaving) were very similar. Unlike RS-COKE, however, in EPSI without temporal interleaving the SW is limited by hardware constraints (slew rate).

Comparing RS-COKE to temporally interleaved EPSI, the latter provided $\sim 30\%$ better SNR efficiency. However,

in practice ^1H temporally interleaved EPSI suffers from aliasing artifacts in the spectrum, arising from residual water signal,²² which limit the temporal interleaving to 3 or fewer interleaves. In RS-COKE, on the other hand, this artifact is practically missing, even in the 5-segmented case.

Nevertheless, the SNR efficiency gap can be further reduced. Several trajectory variations to consider are reducing the size of the overlap region and a different sampling density more resembling the Hann filter, for example, by having the segments overlap at the center of k-space (as k-space is sampled more densely at the

overlaps), and/or switching to radial acquisition in k-space (again, for dense sampling at the center of k-space). In addition, the current implementation treats all segments similarly; thus, extra “overlap” k-space points in the first and last segments—which do not have a segment to overlap with—are essentially discarded and are not used to extend the RO resolution but are used in the convolution regridding. A different reconstruction algorithm—applied after the trajectory corrections have been found—might better use these extra sampling points.

A previous comparison of EPSI with other trajectories⁴³ showed that for most resolutions EPSI has an SNR efficiency higher than spiral, concentric rings, or flyback EPSI, with spiral gaining the upper hand at resolutions below ~4.5 mm. That comparison, however, does not account for filtering of the data or include density-weighted trajectories. Thus, other trajectories, such as density-weighted concentric rings,⁴⁴ may prove more efficient.

Summarizing the above, RS-COKE does not seem to carry an overly excessive penalty in SNR efficiency while also avoiding aliasing in the spectrum. A more thorough investigation, which is outside the scope of the current work, is still required.

Further modification could include the shortening of the water-suppression module, as reported previously.⁹ In addition, the residual motion-induced artifacts could be suppressed by incorporating navigators or other motion-detection methods to reduce signal changes from one excitation to the next.^{45,46} It might also be beneficial to apply dynamic corrections to compensate for magnetic field fluctuations during acquisition,⁴⁷ noting that respiratory-induced field fluctuation is enhanced at 7 T compared to lower field strengths.⁴⁸

5 | CONCLUSION

The artifact-suppressed implementation of RS-COKE reported in this study provides a robust approach to fast MRSI acquisition at 7 T. Unlike standard EPSI, the method is not limited by the increased SW required at ultrahigh field. RO segmentation decouples the spatial resolution from the SW, allowing the technique to use high spatial resolution and exploit the increased SNR at 7 T. RO segmentation comes at a cost of extended total scan duration, but this is compensated by achieving the desired SW and by an SNR increase due to the longer net acquisition time. In addition to RO segmentation, the COKE phase-encoding scheme avoids the Nyquist errors in the spectral domain, which are a further limitation of the EPSI sequence type.


ACKNOWLEDGMENT

We are grateful to Dr. Sagit Shushan (Wolfson Medical Center), Dr. Edna Haran, and the Weizmann Institute's MRI technician team—E. Tegareh and N. Oshri—for assistance in the human imaging scans. We thank Dr. Assaf Tal for the MatLab code to generate the basis sets for LCModel fitting and the scripts to execute the LCModel fitting. Rita Schmidt thanks the generous support of the Joyce Eisenberg Keefer and Mel Keefer Career Development Chair for New Scientists, the Sir Charles Clore Research Prize, Sara Z. de Usansky, and Hinda Machesz Zalc Scheib. The readout-segmented EPSI pulse sequence was originally developed by David Porter and Marco Vicari at the Fraunhofer Institute for Digital Medicine MEVIS. We are grateful to Marco Vicari, Diego Barrios Romero, and Matthias Günther for providing access to this pulse sequence and for their support with this study.

CONFLICT OF INTEREST

A.S. is employed by Siemens Healthcare Ltd, Israel; all other authors declare no competing financial interests. 10-Jun-2022.

ORCID

Rita Schmidt  <https://orcid.org/0000-0003-1580-9964>

REFERENCES

- Gillies RJ, Morse DL. In vivo magnetic resonance spectroscopy in cancer. *Annu Rev Biomed Eng*. 2005;7:287-326.
- Keshavan MS, Stanley JA, Pettegrew JW. Magnetic resonance spectroscopy in schizophrenia: methodological issues and findings—part II. *Biol Psychiatry*. 2000;48:369-380.
- Auer DP, Pütz B, Kraft E, Lipinski B, Schill J, Holsboer F. Reduced glutamate in the anterior cingulate cortex in depression: an in vivo proton magnetic resonance spectroscopy study. *Biol Psychiatry*. 2000;47:305-313.
- Emir UE, Tuite PJ, Öz G. Elevated pontine and putamenal GABA levels in mild-moderate Parkinson disease detected by 7 Tesla proton MRS. *PLoS One*. 2012;7:e30918.
- Emir UE, Auerbach EJ, Moortele PFVD, et al. Regional neurochemical profiles in the human brain measured by 1H MRS at 7 T using local B1 shimming: single-voxel MRS AT 7 T with transceiver array coil. *NMR Biomed*. 2012;25:152-160.
- Mangia S, Tkáč I, Gruetter R, et al. Sensitivity of single-voxel 1H-MRS in investigating the metabolism of the activated human visual cortex at 7 T. *Magn Reson Imaging*. 2006;24:343-348.
- Apšvalka D, Gadie A, Clemence M, Mullins PG. Event-related dynamics of glutamate and BOLD effects measured using functional magnetic resonance spectroscopy (fMRS) at 3T in a repetition suppression paradigm. *Neuroimage*. 2015;118:292-300.
- Ladd ME, Bachert P, Meyerspeer M, et al. Pros and cons of ultra-high-field MRI/MRS for human application. *Prog Nucl Magn Reson Spectrosc*. 2018;109:1-50.

9. Hangel G, Strasser B, Považan M, et al. Ultra-high resolution brain metabolite mapping at 7 T by short-TR Hadamard-encoded FID-MRSI. *Neuroimage*. 2018;168:199-210.
10. Chadzynski GL, Bause J, Shajan G, Pohmann R, Scheffler K, Ehses P. Fast and efficient free induction decay MR spectroscopic imaging of the human brain at 9.4 Tesla: fast MRSI of the human brain at 9.4 Tesla. *Magn Reson Med*. 2017;78:1281-1295.
11. Adalsteinsson E, Irrarrazabal P, Topp S, Meyer C, Macovski A, Spielman DM. Volumetric spectroscopic imaging with spiral-based k-space trajectories. *Magn Reson Med*. 1998;39:889-898.
12. Furuyama JK, Wilson NE, Thomas MA. Spectroscopic imaging using concentric circular echo-planar trajectories in vivo. *Magn Reson Med*. 2012;67:1515-1522.
13. Schirda CV, Tanase C, Boada FE. Rosette spectroscopic imaging: optimal parameters for alias-free, high sensitivity spectroscopic imaging. *J Magn Reson Imaging*. 2009;29:1375-1385.
14. Mansfield P. Spatial mapping of the chemical shift in NMR. *Magn Reson Med*. 1984;1:370-386.
15. Mulkern RV, Panych LP. Echo planar spectroscopic imaging: echo planar spectroscopic imaging. *Concepts Magn Reson*. 2001;13:213-237.
16. Posse S, Otazo R, Dager SR, Alger J. MR spectroscopic imaging: principles and recent advances. *J Magn Reson Imaging*. 2013;37:1301-1325.
17. Porter D., Vicari M. Readout segmentation for increased spectral bandwidth in high spatial and spectral resolution (HiSS) MRI. In Proceedings of the 24th Annual Meeting of ISMRM, Singapore, 2016. p. 1820.
18. Keith G.A., Vicari M., Woodward R.A., Porter D.A. In vivo echo-planar spectroscopic imaging (EPSI) at 7 Tesla with readout segmentation for improved spectral bandwidth. In Proceedings of the 27th Annual Meeting of ISMRM, Montréal, Québec, Canada, 2019. p. 2481.
19. Josephs O, Deichmann R, Turner R. Trajectory measurement and generalised reconstruction in rectilinear EPI. In Proceedings of the 8th Annual Meeting of ISMRM, Denver, CO, 2000. p. 1517.
20. An Z, Tiwari V, Ganji SK, et al. Echo-planar spectroscopic imaging with dual-readout alternated gradients (DRAG-EPSI) at 7 T: application for 2-hydroxyglutarate imaging in glioma patients. *Magn Reson Med*. 2018;79:1851-1861.
21. Posse S, DeCarli C, Le Bihan D. Three-dimensional echo-planar MR spectroscopic imaging at short echo times in the human brain. *Radiology*. 1994;192:733-738.
22. Bogner W, Otazo R, Henning A. Accelerated MR spectroscopic imaging—a review of current and emerging techniques. *NMR Biomed*. 2021;34:e4314.
23. Webb P, Spielman D, Macovski A. A fast spectroscopic imaging method using a blipped phase encode gradient. *Magn Reson Med*. 1989;12:306-315.
24. Schmidt R, Seginer A, Tal A. Combining multiband slice selection with consistent k-t-space EPSI for accelerated spectral imaging. *Magn Reson Med*. 2019;82:867-876.
25. Keith G.A., Seginer A., Porter D.A., Schmidt R. Echo-planar spectroscopic imaging with readout-segmented COKE at 7T: artifact analysis using a purpose-built phantom and simulation. In Proceedings of the 29th Annual Meeting of the ISMRM, Virtual Conference, 2021. p. 2207.
26. Balchandani P, Spielman D. Fat suppression for 1H MRSI at 7T using spectrally selective adiabatic inversion recovery. *Magn Reson Med*. 2008;59:980-988.
27. Henning A, Fuchs A, Murdoch JB, Boesiger P. Slice-selective FID acquisition, localized by outer volume suppression (FIDLOVS) for ¹H-MRSI of the human brain at 7 T with minimal signal loss. *NMR Biomed*. 2009;22:683-696.
28. Hangel G, Strasser B, Považan M, et al. Lipid suppression via double inversion recovery with symmetric frequency sweep for robust 2D-GRAPPA-accelerated MRSI of the brain at 7 T. *NMR Biomed*. 2015;28:1413-1425.
29. Mugler JP, Brookeman JR. Off-resonance image artifacts in interleaved-EPI and GRASE pulse sequences. *Magn Reson Med*. 1996;36:306-313.
30. Porter DA, Heidemann RM. High resolution diffusion-weighted imaging using readout-segmented echo-planar imaging, parallel imaging and a two-dimensional navigator-based reacquisition. *Magn Reson Med*. 2009;62:468-475.
31. Tkáč I, Starčuk Z, Choi I-Y, Gruetter R. In vivo ¹H NMR spectroscopy of rat brain at 1 ms echo time. *Magn Reson Med*. 1999;41:649-656.
32. Bruder H, Fischer H, Reinfelder H-E, Schmitt F. Image reconstruction for echo planar imaging with nonequidistant k-space sampling. *Magn Reson Med*. 1992;23:311-323.
33. Hall EL, Stephenson MC, Price D, Morris PG. Methodology for improved detection of low concentration metabolites in MRS: optimised combination of signals from multi-element coil arrays. *Neuroimage*. 2014;86:35-42.
34. Jackson JI, Meyer CH, Nishimura DG, Macovski A. Selection of a convolution function for Fourier inversion using gridding (computerised tomography application). *IEEE Trans Med Imaging*. 1991;10:473-478.
35. Harris FJ. On the use of windows for harmonic analysis with the discrete Fourier transform. *Proc IEEE*. 1978;66:51-83.
36. Provencher SW. Estimation of metabolite concentrations from localized in vivo proton NMR spectra. *Magn Reson Med*. 1993;30:672-679.
37. Provencher SW. LCModel. Accessed July 3, 2022. <http://s-provencher.com/lcmodel.shtml>.
38. Považan M, Hangel G, Strasser B, et al. Mapping of brain macromolecules and their use for spectral processing of 1 H-MRSI data with an ultra-short acquisition delay at 7 T. *Neuroimage*. 2015;121:126-135.
39. Jona G, Furman-Haran E, Schmidt R. Realistic head-shaped phantom with brain-mimicking metabolites for 7 T spectroscopy and spectroscopic imaging. *NMR Biomed*. 2021;34:e4421.
40. Nassirpour S, Chang P, Henning A. High and ultra-high resolution metabolite mapping of the human brain using 1 H FID MRSI at 9.4T. *Neuroimage*. 2018;168:211-221.
41. Schmidt R., Seginer A., Tal A. Combining multi-band slice selection with COKE (COherent K-t-space EPSI) for accelerated spectral imaging. In Proceedings of the 26th Annual Meeting of ISMRM, Paris, France, 2018. p. 1059.
42. Kasper L, Haeberlin M, Dietrich BE, et al. Matched-filter acquisition for BOLD fMRI. *Neuroimage*. 2014;100:145-160.
43. Jiang W, Lustig M, Larson PEZ. Concentric rings K-space trajectory for hyperpolarized (¹³C) MR spectroscopic imaging. *Magn Reson Med*. 2016;75:19-31.

44. Chiew M, Jiang W, Burns B, et al. Density-weighted concentric rings k -space trajectory for ^1H magnetic resonance spectroscopic imaging at 7 T. *NMR Biomed*. 2018;31:e3838.
45. Zaitsev M, Dold C, Sakas G, Hennig J, Speck O. Magnetic resonance imaging of freely moving objects: prospective real-time motion correction using an external optical motion tracking system. *Neuroimage*. 2006;31:1038-1050.
46. Hoinkiss DC, Porter DA. Prospective motion correction in 2D multishot MRI using EPI navigators and multislice-to-volume image registration: prospective MoCo using multislice-to-volume registration. *Magn Reson Med*. 2017;78:2127-2135.
47. Keating B, Ernst T. Real-time dynamic frequency and shim correction for single-voxel magnetic resonance spectroscopy: dynamic shimming for MR spectroscopy. *Magn Reson Med*. 2012;68:1339-1345.
48. Van de Moortele P-F, Pfeuffer J, Glover GH, Ugurbil K, Hu X. Respiration-induced B0 fluctuations and their spatial distribution in the human brain at 7 Tesla. *Magn Reson Med*. 2002;47:888-895.

SUPPORTING INFORMATION

Additional supporting information may be found in the online version of the article at the publisher's website.

Figure S1: Comparison of the effect different reconstruction steps have. Shown are NAA images after a different correction step was skipped each time, along with the NAA image after the full correction (right most). Top, phantom results and bottom, in vivo results. The correction steps, from left to right are (in parentheses the relevant section names in main text): smoothing of signal at overlaps ('Residual segment inconsistencies'), segment trajectory corrections ('Trajectory corrections (k_x and time t)'), phase correction *between* segments ('Phase difference between segments'), phase correction *within* segments ('Phase difference within segments'), and even/odd RO corrections ('Even/Odd inconsistencies — Nyquist ghosts'). The scans reconstructed are the same as in **Fig. 6** (phantom) and **Fig. 7** (in vivo) of the main text (using, however, slightly different masks).

Figure S2: NAA images before (a) and after (b) RO-segments correction. The images show (from left to right) – NAA integral map, LCModel NAA map, and the matching LCModel CRLB map. c) Spectra from two voxels (marked as (1) and (2) on the left image) are shown before and after correction with LCModel fitting. It can be seen that fitting the baseline can reduce the artifact effect.

Figure S3: The integrand, $\sum_i \eta_i(\mathbf{k}) \cdot d_{\text{target}}^2(\mathbf{k})/d_{i,\text{acq}}(\mathbf{k})$, from Eq. s8 for sequence variations using SW = 2941 Hz, FOV 280 mm, and dead time of 25 μs , based on three segments with overlaps of size of 8 k-samples. The integrand is proportional to the signal's noise variance at each RO k -position. Left, without Hann filter, and right, with.

Figure S4: The integrand, $\sum_i \eta_i(\mathbf{k}) \cdot d_{\text{target}}^2(\mathbf{k})/d_{i,\text{acq}}(\mathbf{k})$, from Eq. s8 for sequence variations using SW = 2941 Hz, FOV 280 mm, and dead time of 25 μs , based on three segments without overlaps. The integrand is proportional to the signal's noise variance at each RO k -position. Left, without Hann filter, and right, with.

Figure S5: The integrand, $\sum_i \eta_i(\mathbf{k}) \cdot d_{\text{target}}^2(\mathbf{k})/d_{i,\text{acq}}(\mathbf{k})$, from Eq. s8 for sequence variations using SW = 2000 Hz, FOV 280 mm, and dead time of 25 μs , based on three segments without overlaps. The integrand is proportional to the signal's noise variance at each RO k -position. Left, without Hann filter, and right, with.

Figure S6: The integrand, $\sum_i \eta_i(\mathbf{k}) \cdot d_{\text{target}}^2(\mathbf{k})/d_{i,\text{acq}}(\mathbf{k})$, from Eq. s8 for two different acquisition dead times of 25 μs (solid lines) and 0.1 μs (dashed lines). Left, without Hann filter, and right, with. Sequences shown are variations of the human imaging case (iv): SW = 3571 Hz (echo spacing 280 μs), FOV 260 mm, and based on three segments with overlaps of size of 8 k-samples. The integrand is proportional to the signal's noise variance at each RO k -position. Outside the overlaps and without the Hann filter the plots are proportional to the RO gradient used.

Table S1: Relative SNR efficiency of different RS-COKE and EPSI variations using SW = 2941 Hz, FOV 280 mm, and dead time of 25 μs , based on three segments with overlaps of size of 8 k-samples. SNR efficiencies are normalized relative to the 3-segmented RS-COKE case. All variations had the same total scan time, same SW, same FOV, same resolution (spatial and spectral), same echo-train length, and same TR. Thus, $1/\sqrt{|\sigma_{\text{final}}|_2^2}$ based on Eq. s8 could also be used for a relative SNR efficiency measure.

Table S2: Relative SNR efficiency of different RS-COKE and EPSI variations using SW = 2941 Hz, FOV 280 mm, and dead time of 25 μs , based on three segments without overlaps. SNR efficiencies are normalized relative to the 3-segmented RS-COKE case. All variations had the same total scan time, same SW, same FOV, same resolution (spatial and spectral), same echo-train length, and same TR. Thus, $1/\sqrt{|\sigma_{\text{final}}|_2^2}$ based on Eq. s8 could also be used for a relative SNR efficiency measure.

Table S3: Relative SNR efficiency of different RS-COKE and EPSI variations using SW = 2000 Hz, FOV 280 mm, and dead time of 25 μs , based on three segments without overlaps. SNR efficiencies are normalized relative to the 3-segmented RS-COKE case. All variations had the same total scan time, same SW, same FOV, same resolution (spatial and spectral), same echo-train length, and same TR. Thus, $1/\sqrt{|\sigma_{\text{final}}|_2^2}$ based on Eq. s8 could also be used for a relative SNR efficiency measure.

Table S4: SNR efficiency gain as a percentage if acquisition dead time (reserved for PE gradients in RS-COKE) were reduced from 25 μs to 0.1 μs (the dead time appears both at

the start and end of each gradient lobe). Cases listed (left column) are the human imaging scan cases given in the main text, where the '+' signifies modifications on top of the original case. Below each case appear its main parameters, echo spacing (ESP), number of segments, RO FOV, and RO reconstruction resolution (pixels). For every basic setup – defined by the SW, resolution (spatial and spectral), and number of segments of RS-COKE – three sequences were compared: RS-COKE with sine-shaped RO gradients (as implemented in this work), RS-COKE using trapezoid RO gradients, and temporally interleaved EPSI. For n-segmented RS-COKE, the echo-spacing of the matching

EPSI was n times larger but used n temporal interleaves. For each case and sequence, two SNR gains are given, on the left, without applying a Hann filter and on the right, with.

How to cite this article: Seginer A, Keith GA, Porter DA, Schmidt R. Artifact suppression in readout-segmented consistent K-t space EPSI (RS-COKE) for fast ¹H spectroscopic imaging at 7 T. *Magn Reson Med.* 2022;88:2339-2357. doi: 10.1002/mrm.29373